

Theoretical Design by First Principles Molecular Dynamics of a Bioinspired Electrode–Catalyst System for Electrocatalytic Hydrogen Production from Acidified Water

Federico Zipoli,^{*,†} Roberto Car,^{‡,§} Morrel H. Cohen,^{†,§} and Annabella Selloni^{*,†}

Department of Chemistry and Princeton Institute for the Science and Technology of Materials, Princeton University, Princeton, New Jersey 08544, and Department of Physics and Astronomy, Rutgers University, Piscataway, New Jersey 08854

Received June 11, 2010

Abstract: Bacterial di-iron hydrogenases produce hydrogen efficiently from water. Accordingly, we have studied by first-principles molecular-dynamics simulations (FPMD) electrocatalytic hydrogen production from acidified water by their common active site, the [FeFe]_H cluster, extracted from the enzyme and linked directly to the (100) surface of a pyrite electrode. We found that the cluster could not be attached stably to the surface via a thiol link analogous to that which attaches it to the rest of the enzyme, despite the similarity of the (100) pyrite surface to the Fe₄S₄ cubane to which it is linked in the enzyme. We report here a systematic sequence of modifications of the structure and composition of the cluster devised to maintain the structural stability of the pyrite/cluster complex in water throughout its hydrogen production cycle, an example of the molecular design of a complex system by FPMD.

1. Introduction

There is currently a great deal of scientific and technological interest in the photo- or electrocatalytic production of hydrogen from water. Metallic platinum has suitably high catalytic activity with a turnover number on the order of 10³ per second but is too rare and expensive an element for large-scale deployment. A correspondingly active catalyst comprised of earth-abundant elements is needed. Now, the hydrogen evolution reaction 2H⁺ + 2e⁻ → H₂ is a central process in the global biological energy cycle. It is mediated by three different classes of enzymes with multiple subgroups.^{1,2} Of these, the di-iron hydrogenases found in hydrogen-producing microorganisms have the highest turnover frequency, over 9000 H₂ molecules per second at room temperature, almost an order of magnitude faster than that

of Pt.² These enzymes have been extensively studied both theoretically^{3–13} and experimentally.^{14–24} Removed from the protein environment, their active site, the [FeFe]_H cluster, could be an attractive candidate for a catalyst for hydrogen production from water by electro- or photocatalysis.²⁵ It is composed of abundant elements and is small enough to pack densely. However, it seems unlikely that the [FeFe]_H cluster could, without changes in its structure and composition, retain its hydrogen production activity and remain structurally stable throughout its catalytic production cycle when removed from its specialized, protected environment within the enzyme and exposed to water. To explore the needed changes, we have carried out a theoretical study of hydrogen production by the active center of the di-iron enzyme, starting with the bare [FeFe]_H cluster detached from the enzyme without a change in structure or composition, linked to a pyrite surface acting as an electrode, and immersed in acidified water. We modeled this functionalized surface and investigated its stability and catalytic properties using static density functional theory (DFT) calculations and first-principles molecular-dynamics (FPMD) simulations.²⁶ The pyrite surface was chosen because its atomic structure is compatible with that

* To whom correspondence should be addressed. E-mail: fzipoli@princeton.edu (F.Z.).

† Department of Chemistry, Princeton University.

‡ Princeton Institute for the Science and Technology of Materials, Princeton University.

§ Rutgers University.

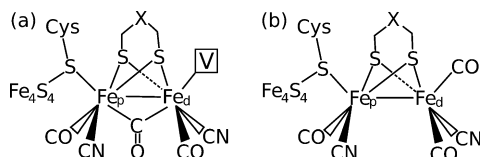


Figure 1. Sketches of the active center of di-iron hydrogenase in the bridging (a) and in the terminal (b) configurations. In a, the configuration in the enzyme, the distal iron has a vacant site, indicated by V, which can coordinate ligands such as CO, H₂O, etc. The “X” in the chelating S—CH₂—X—CH₂—S group stands for CH₂, NH, or O.¹⁸

of the [FeFe]_H cluster and *a priori* suggests the possibility of stable linkage and easy electron transfer to the cluster. Not surprisingly, we found that the [FeFe]_H cluster did not remain structurally stable in contact with acidified water during the course of its hydrogen production cycle. We then initiated a systematic search for structural and compositional modifications which could establish stability while maintaining suitable hydrogen production activity. We found that it is indeed possible to realize a strongly linked cluster configuration on the pyrite surface able to produce hydrogen efficiently and stably from acidified water. The details of the hydrogen production cycle of that configuration are reported elsewhere.²⁷ Here, we report the detailed numerical studies and analyses of the sequence of changes leading to the successful configuration, a process of scientific interest in its own right and, more generally, an illustration of the potential of FPMD for the molecular design of quite complicated chemical systems.

In the [FeFe]_H cluster, two iron atoms are coordinated with CO and CN ligands and bridged by a chelating group, S—CH₂—X—CH₂—S, where X can be a NH (DTMA) or CH₂ (PDT) group, cf. Figure 1a.²⁰ In the enzyme, one of the two iron atoms, the proximal iron (Fe_p), is connected to an iron–sulfur cluster (a cubane) via the *sulfur* of a cysteine.²⁰ The other iron is the distal iron (Fe_d). Two important groups of isomers have been identified,^{4,28} CO-bridging (μ -CO) and CO-terminal (CO_T). They differ in the position of one of the CO ligands. In CO_T, each CO is connected to only one of the two iron atoms, while in μ -CO, the configuration of the active ready state of the enzyme,¹⁸ there is one CO bridging the two iron atoms leaving a vacant coordination site V on Fe_d. In previous work,²⁹ we showed that the CO-bridging configuration had to be stable for the [FeFe]_H cluster of hydrogenase to function as an efficient hydrogen-production catalyst. We found that in vacuo, however, the CO-terminal configuration was slightly more stable and would effectively stop catalytic action. Since in practical applications the cluster would be immersed in acidified water, we subsequently studied³⁰ the effects of a water environment on its structure and reactivity. The electrons were added without considering the electrode explicitly. The main advantages of the model used in ref 30 were that the electrostatic effects, the dynamics of the proton diffusion in water via the Grotthuss-shuttle mechanism, and the proton sharing between the cluster and the water molecules were all taken into account in the FPMD computations. The main results were that (i) interconversion between the bridging and terminal configurations occurs without significant activation energies; (ii) the presence of terminal isomers does not stop the catalytic activity because a local hydrophobicity kinetically prevents the formation of a low-energy CO_T isomer in which a proton bridges the two Fe atoms (μ -H); (iii) there are at least three different pathways for H₂ production by the bridging configuration which involve a sequential protonation of Fe_d only or of both Fe_d and DTMA; and (iv) the bare active center of the di-iron hydrogenases can be an efficient catalyst for H₂ production provided that electrons are transferred to the cluster. However, we also found (v) that when the cluster is detached from the enzyme and immersed in acidified water, there are configurations in which the bond between Fe_p and the linking sulfur is weak and can break. The stability of the link between the electrode and the di-iron cluster thus emerged as a key issue in the design of a viable system. Accordingly, in the present work, we first focused our simulations on the linkage between the catalyst and FeS₂(100), the most stable surface of pyrite. We searched for structural and minor compositional modifications of [FeFe]_H which would lead to stable attachment while preserving the vacant coordination site on Fe_d in a configuration which exposed it to the water. We found such a configuration, one which formed a strong tridentate link to the surface, as described in section 3, and produced hydrogen successfully, as described in section 4.2. However, during the course of the cycle, the link of Fe_p to the chelating bridge was susceptible to breaking upon protonation of the bridging sulfur, which is exposed to the water, as described in section 5.1. Substitution of a PH group for that S eliminated the instability and maintained the hydrogen production capability, as discussed in section 5.2. We denoted the resulting cluster [FeFe]_P because of the importance of the phosphorus substitution, and we give an account here of our systematic transformation of [FeFe]_H from its in-the-enzyme configuration to [FeFe]_P linked to FeS₂(100).

2. Methods

Our study is based on Car–Parrinello (CP)²⁶ FPMD simulations of the [FeFe]_H cluster in a liquid-water environment with or without hydronium ions. The FPMD simulations were performed within the framework of density-functional theory in the local-spin-density approximation supplemented by generalized-gradient corrections³¹ as implemented in the CP code of the Quantum-ESPRESSO package.³² We employed ultrasoft pseudopotentials^{33,34} with plane-wave expansions of the Kohn–Sham orbitals and the augmented density up to kinetic energy cutoffs of 30 and 240 Ry, respectively. The pyrite electrode was modeled in a slab geometry with (100) surfaces and 3D periodic boundary conditions at the experimental lattice constant, 5.428 Å.³⁵ (Our theoretical lattice constant, computed with fully converged Brillouin zone (BZ) sampling, is 5.404 Å, only 0.4% shorter than the experimental one.) We used a 2 × 2 supercell having the ideal bulk termination of the slab. The slab was nine-atomic-layers-thick (24 FeS₂ units, cf. Figure 2) in a tetragonal simulation box with $a = 10.856$ Å and $c = 21.712$ Å with a vacuum width between slabs of 15 Å. The atoms of the three bottom layers were fixed to their positions in the clean

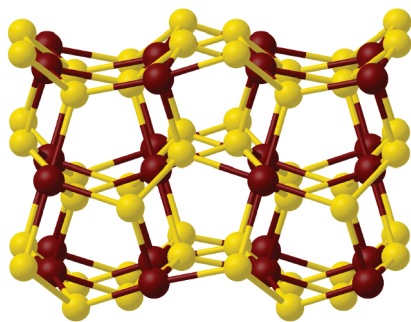


Figure 2. Side view of the FeS_2 (100) surface modeled in a geometry having a slab nine-atomic-layers-thick separated by 15 Å of vacuum in a tetragonal simulation box with $a = 10.856$ Å and $c = 21.712$ Å. Fe atoms are dark red, and S atoms are yellow.

surface during geometric optimizations of the supported catalyst, whereas all atoms were free to move during the FPMD simulations. We used only the Γ point to sample the surface BZ for both FPMD and structural optimizations. Test calculations comparing the results of the Γ -point integration with those of a k -point mesh showed differences in relative energies on the order of $k_B T$. We attached a sequence of progressively further modified di-iron $[\text{FeFe}]_H$ clusters (see section 3) to the $\text{FeS}_2(100)$ surface and added 37 water molecules between slabs to simulate immersion of the supported cluster in water of real density. A fictitious electronic mass of 350 au and a time step of 0.072 fs were used in the FPMD simulations. The deuterium mass was used for hydrogen to allow for a longer time step. Constant temperature was imposed on the ions by a Nosé–Hoover thermostat.³⁶ In situations where the system's HOMO–LUMO energy gap was “small” (less than 0.1 eV), adiabaticity of the FPMD trajectory was maintained by coupling two separate Nosé–Hoover thermostats to the nuclear and electronic subsystems.³⁷ Static calculations on the isolated $[\text{FeFe}]_H$ cluster in vacuo were performed using the PW code of the Quantum-ESPRESSO package.³² Energy barriers were calculated using the climbing-image nudged-elastic-band (NEB)³⁸ and string methods.³⁹ For geometry optimizations and energy-barrier determinations, the norm of the force vector was required to be smaller than 5 meV/Å at convergence. Different pseudopotentials were used for the iron atoms of the cluster and for those of the pyrite slab, with 16 and 8 electrons explicitly treated as valence electrons, respectively. This choice reduced the computational cost without affecting the accuracy of our description of the delicate chemistry involving the two iron atoms of the $[\text{FeFe}]_H$ or $[\text{FeFe}]_P$ cluster. The validity of DFT for addressing the electronic and chemical properties of the FeS_2 surface^{40–43} and the di-iron cluster in different environments is well established.^{3–12,29,30} Because the duration of our simulations is limited to a few picoseconds, each computed trajectory may remain sensitive to the initial conditions imposed. To overcome this possible source of bias, we normally compute several trajectories spanning a representative range of initial conditions.

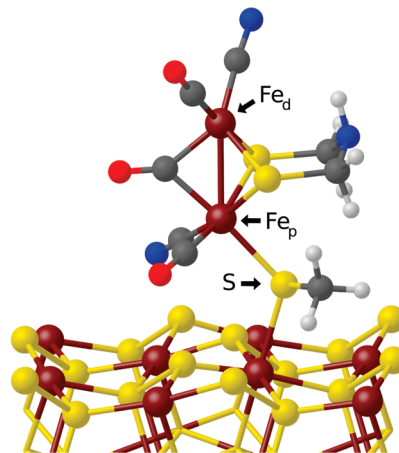


Figure 3. Hypothetical geometry of the $[\text{FeFe}]_H$ cluster linked to a (100) FeS_2 surface via a linking S atom, labeled S. The distal and the proximal iron are indicated by the labels Fe_d and Fe_p , respectively. Fe_p and Fe_d are bridged by di(thiomethyl)amine (DTMA, $\text{S}-\text{CH}_2-\text{NH}-\text{CH}_2-\text{S}$). Fe atoms are dark red. S atoms are yellow. C atoms are dark gray. N atoms are blue. O atoms are red. H atoms are light gray. The cluster atoms and the surface atoms are represented by balls and sticks. The remaining slab atoms are represented by cylinders.

3. Model

3.1. $\text{FeS}_2(100)$ Surface. The stoichiometric (100) surface of pyrite is formed by breaking the Fe–S bonds between adjacent (100) atomic layers while keeping the sulfur-dimer units intact. The S and Fe atoms on the FeS_2 surface are three- and 5-fold coordinated, respectively, whereas they are four- and 6-fold coordinated in the bulk. The LUMO of the clean defect-free surface derives from the d_z^2 orbitals of the surface iron atoms, and the computed band gap is 0.50 eV (0.42 eV for bulk pyrite, compared to the experimental value of ~ 0.9 eV,⁴⁴ a typical DFT underestimate, not of concern in the present studies).

Water adsorption on the FeS_2 (100) surface has been extensively studied both theoretically^{40,43,45–47} and experimentally,^{48,49} see refs 50 and 51 and references therein. In agreement with these previous studies, we found that water adsorbs in molecular form via a coordinative covalent bond between a lone-pair orbital of its oxygen and an empty d_z^2 orbital of a surface iron atom. The computed adsorption energy is 0.57 eV at low (1/8 ML) coverage. Due to intermolecular H-bond formation, this binding energy increases slightly with increasing coverage and becomes 0.62 eV at full (1 ML) coverage.

3.2. Supported Catalyst. Failure of Terminating Thiol Linkages. In modeling the $[\text{FeFe}]_H$ cluster in our earlier works,^{29,30} we followed the common procedure of replacing the cysteine linking Fe_p to the cubane within the enzyme by a methylthiol as in Figure 1b. In analogy with the link between the $[\text{FeFe}]_H$ cluster and the cubane in the enzyme, it is possible to attach the catalyst to the pyrite surface using the sulfur atom (S) of that SCH_3 to connect Fe_p to one of the surface Fe atoms ($\text{Fe}_{\text{surf}1}$). A sketch of this configuration is shown in Figure 3. We optimized its geometry in vacuo and found in addition that the CN group connected to Fe_p

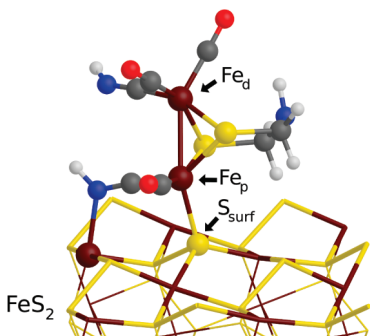


Figure 4. Optimized geometry of the active center of the $[FeFe]_H$ subcluster of the hydrogenase connected to the pyrite surface via a Fe_p – S_{surf} bond. The SCH_3 group connected to Fe_p has been removed so that Fe_p can be connected directly to S_{surf} . The N atom of $(CN)_p$ is connected to a surface Fe atom via a dative bond. The cluster is in the terminal configuration. The color code and the labels are those of Figure 3.

$((CN)_p)$, which lies close to the surface, can easily make a dative bond with a nearby Fe atom (Fe_{surf2}). Binding the SCH_3 to Fe_{surf1} restores the 6-fold coordination the latter would have had in the bulk, which leads to a relatively short Fe_{surf1} –S distance, 2.4 Å. Upon protonation of Fe_d during the course of the H_2 production cycle, however, the Fe_p –S bond breaks. This is analogous to the weakening of the Fe_p – SCH_3 link observed on protonation of the methylthiolate in water in the absence of the electrode,³⁰ with the Fe_{surf1} –S bond playing the role of the thiolate protonation. To increase the stability of the Fe_p –S bond, we removed the CH_3 group connected to the linking sulfur, which is then 2-fold coordinated. We found that this sulfur is usually deprotonated in water;³⁰ nevertheless, the Fe_p –S bond breaks when the sulfur occasionally does become protonated. We conclude that an Fe_p –S– Fe_{surf1} linkage is not stable. The fact that an analogous thiol linkage does occur in the enzyme suggests that the enzyme pocket provides the stabilization.

Dispensing with the Added Thiol; Protonation of the CN's. To circumvent the above problems, we removed the SCH_3 group entirely and connected the Fe_p directly to a sulfur atom on the pyrite surface, S_{surf} , in effect substituting S_{surf} for the linking sulfur of the enzyme. As the S atoms on the surface are undercoordinated, this link to Fe_p restores the bulk 4-fold coordination of S_{surf} . A further stabilization of 0.38 eV is provided by the interaction between the N atom of $(CN)_p$ and an Fe atom on the surface. In addition, the CN groups connected to both Fe_p and Fe_d , $(CN)_p$ and $(CN)_d$, are protonated, as usually found in water.³⁰ The optimized geometry is shown in Figure 4. The Fe_p – S_{surf} bond length is 2.243 Å, even shorter than the bulk Fe–S separation, 2.264 Å. However, only CO_T is stable in this linking geometry; μ -CO is unstable and converts to CO_T . The strong Fe_p – S_{surf} bond destabilizes the bond between the Fe_p and the μ -CO group bridging the two iron atoms by withdrawing electron density from the Fe_p –(μ -CO) bond. We conclude that a further modification of the cluster is needed as there is no vacant coordination site exposed to the water and available for hydrogen production.

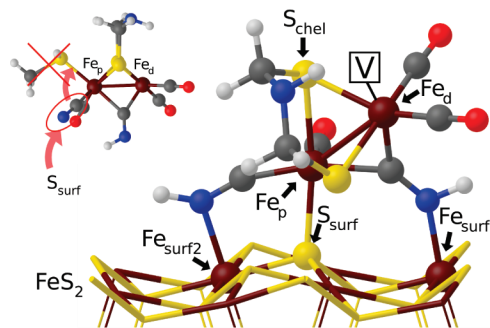


Figure 5. Optimized geometry of the μ –($CN)_d$ –H configuration (inset) when the N atom of $(CN)_d$ is linked to a surface Fe atom (Fe_{surf1}) via a dative bond. $(CN)_p$ –H is linked to another surface iron (Fe_{surf2}) via another dative bond. To allow linkage of both $(CN)_d$ and Fe_p to the surface, the coordination of $(CN)_p$ to Fe_p has been changed, as indicated by the upper red arrow in the inset. Fe_p is linked to a surface S atom (S_{surf}) as indicated by the lower red arrow in the inset. The bonds of Fe_p and $(CN)_d$ with the surface stabilize the bridging configuration with V-up. The result is a tridentate anchoring of the cluster to the surface. S_{chel} is the upper bridging thiol, that further from the surface. Note that S_{chel} is opposite S_{surf} along an approximate octahedral coordination axis of Fe_p . The color code and the labels are those of Figure 3.

Adopting the μ –($CN)_d$ –H Configuration. In ref 30, we reported observing an unusual structure, one with the protonated $(CN)_d$ bridging the two iron atoms (the μ –($CN)_d$ –H configuration), during an FPMD simulation at $T = 300$ –350 K in water, cf. Figure 6d of ref 30 and the inset in Figure 5. The spontaneous formation of this isomer suggests that its energy is close to those of the μ -CO and CO_T isomers. We find that this novel isomer can form a stable link with the $FeS_2(100)$ surface. In the resulting adsorption geometry, the dative bond between the N of the μ –($CN)_d$ –H and a surface Fe atom (Fe_{surf}) locks the system into the bridging configuration with the vacancy on Fe_d in the “up” position (V-up) as needed for H_2 production, Figure 5, eliminating the lability found for the isolated cluster in water.⁴ To bring the μ –($CN)_d$ –H close enough to the surface for that bond to form, we had to move the $(CN)_p$ –H to the Fe_p coordination site vacated by the methylthiol. An Fe_p – S_{surf} bond then formed at the coordination site vacated by CN_p , while an additional dative bond forms between the N of $(CN)_p$ –H and another surface Fe. This tridentate adsorption geometry is more stable by 0.51 eV than that of the CO_T isomer shown in Figure 4. The bonding of Fe_p to S_{surf} restores the bulk coordination of S_{surf} and is consequently strong, with a bond length of 2.271 Å close to the 2.264 Å Fe–S bond length of the bulk. Fe_p has an approximately octahedral coordination shell in which S_{surf} and that S of the dithiol bridge which is further from the surface, S_{chel} , are at opposite ends of one of the three octahedral axes, cf. Figure 5. Elementary ligand theory tells us that introducing asymmetry by strengthening one bond on an axis weakens the opposite bond on that axis. The Fe_p – S_{chel} bond is indeed longer, 2.381 Å, a significant result we return to in section 5.

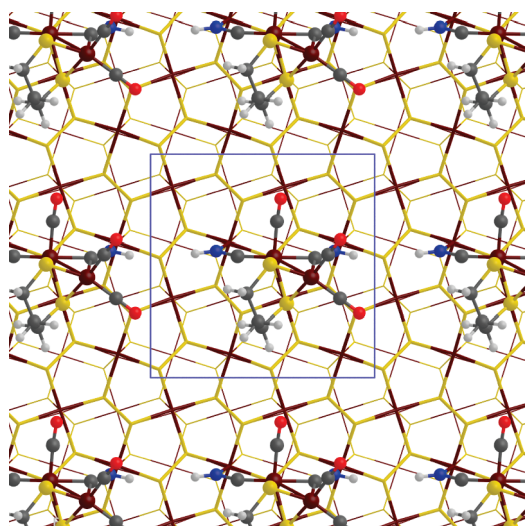


Figure 6. Top view of the μ -(CN)_d-H isomer described in Figure 5. But here, the chelating group DTMA has been replaced by PDT (see text). The structure has been replicated in the (*x,y*) plane to show the periodicity of the slab and the distance between the images. The edges of the tetragonal cell in the (*x,y*) plane are indicated by blue lines. The color code is that of Figure 3. Only the atoms of the cluster are indicated by balls and sticks.

Modifying the Chelating Bridge. To improve further the stability of the supported cluster, we have also changed the chelating group from di(thiomethyl)amine (DTMA, S-CH₂-NH-CH₂-S)^{29,30} to 1,3-propanedithiolate (PDT, S-CH₂-CH₂-CH₂-S). In vacuo, we found that protonation of DTMA modifies the HOMO charge density. When DTMA is not protonated, or analogously DTMA is replaced by PDT, the HOMO is mainly localized on the iron atoms on the pyrite surface. On the other hand, after the protonation of DTMA, 6% and 10% of the HOMO charge density is localized on Fe_p and S_{chel}, respectively. This modification of the charge weakens the Fe_p-S_{chel} bond, which increases in length from 2.37 Å to 2.48 Å. Since DTMA is protonated easily and stably,³⁰ by replacing DTMA with PDT, we both make the Fe_p-S_{chel} bond more stable and eliminate the competition for the first protonation between the amine of DTMA and Fe_d.

A Model Suitable for Simulating H₂ Production. Top and side views of the resulting model, a modified [FeFe]_H cluster with a PDT bridge supported on a (100) surface of the pyrite slab, are shown in Figures 5, 6, and 7a. The modified di-iron cluster occupies roughly half of the surface of the simulation cell used here, thus modeling a densely functionalized surface, cf. Figure 6. The distance of closest approach between the cluster replicas is 3.2 Å, the separation between the H atoms of the (CN)_d of one cluster and of the (CN)_p of its neighbor. The use of this simulation cell allows studying H₂ formation at high coverage within an affordable computation time.

3.3. Water Environment. The water environment was modeled using 37 water molecules, either without an extra proton (“neutral water”) or with one (“acidified water”). Excluding the volume of the slab, estimated from the pyrite bulk density, and that of the cluster, estimated from tabulated

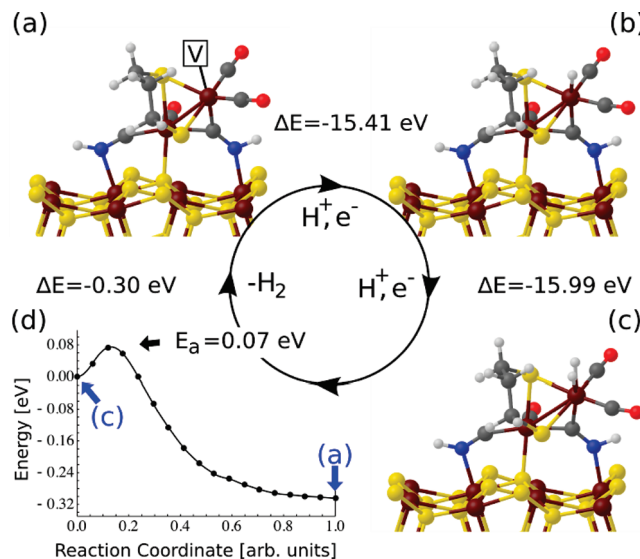


Figure 7. Catalytic cycle in vacuo for H₂ production by the μ -(CN)_d-H isomer with PDT. (a) Starting configuration with a vacant site on Fe_d. (b) The first H atom has been added to Fe_d. (c) The second H atom has been added to Fe_d. ΔE indicates the energy change (in eV), and (d) E_a is the energy barrier encountered during desorption of a H₂ molecule along the minimum-energy path computed via the NEB method. The continuous black line represents a cubic interpolation. The color code is that of Figure 3.

van der Waals radii, the density of 37 H₂O molecules within our simulation cell is close to the density of water at standard conditions. Our explicit quantum treatment of the water molecules not only takes into account important electrostatic effects but also provides a description of proton diffusion in water⁵² and of proton sharing between the cluster and water. As demonstrated previously,³⁰ all of these aspects are important for a more realistic representation of the system and its dynamics.

4. H₂ Production by the Model-Supported Catalyst

4.1. Production of H₂ in Vacuo. We addressed the pathway for hydrogen production by the FeS₂(100)-supported μ -(CN)_d-H model cluster in vacuo as preliminary to our investigation of H₂ production in water. In our previous studies,^{29,30} H₂ production occurred by two sequential reductions and protonations of the distal iron. To analyze the electron flow within the system and the effect of protonation upon that flow, we continue this step by step procedure here. In particular, we analyze changes of the electron density upon the same sequential reductions and protonations. However, we compute energy differences only between the neutral systems resulting after both the electron and proton have been added, the energies of which are well-defined in unbounded periodic systems. In the next section, where the water environment is taken into account, we discuss how electrons are transferred dynamically to Fe_d from the electrode during coordinated dynamic proton transfers from the acidified water to the cluster.

There are three main stages of the cycle: after desorption of H₂ and before hydrogenation of Fe_d, singly hydrogenated

Table 1. Relevant Bond Lengths (\AA) during the Cycle in Vacuo for $[\text{FeFe}]_{\text{H}}$, $\text{H}[\text{FeFe}]_{\text{H}}$, and $\text{HH}[\text{FeFe}]_{\text{H}}$, cf. Figs. 7a–c, respectively

	$\text{Fe}_p\text{—Fe}_d$	$\text{N}\text{—Fe}_{\text{surf}}$	$\text{Fe}_d\text{—H}$	$\text{Fe}_p\text{—S}_{\text{surf}}$	$\text{Fe}_p\text{—C of } (\mu\text{-(CN)}_d)$	$\text{Fe}_d\text{—C of } (\mu\text{-(CN)}_d)$
$[\text{FeFe}]_{\text{H}}$	2.52	2.03		2.27	1.99	1.84
$\text{H}[\text{FeFe}]_{\text{H}}$	2.57	2.03	1.54	2.32	1.94	1.95
$\text{HH}[\text{FeFe}]_{\text{H}}$	2.89	2.05	1.73, 1.74	2.28	1.94	1.98

Table 2. Relevant Charges (In Units of the Proton Charge $e = 1.6 \times 10^{-19} \text{ C}$) and Electron-Number Changes in the $[\text{FeFe}]_{\text{H}}$, $\text{H}[\text{FeFe}]_{\text{H}}$, and $\text{HH}[\text{FeFe}]_{\text{H}}$ Intermediates of the Cycle in Vacuo, cf. Figure 8^a

	change of electron number		charge			
	ΔN_{slab}	$\Delta N_{\text{cluster}}$	Fe_d	Fe_p	1st H	2nd H
$[\text{FeFe}]_{\text{H}}$, Figure 8a			−0.56	−0.66		
$[\text{FeFe}]_{\text{H}}^{-1}$, Figure 8b	+0.74	+0.19	−0.59	−0.66		
$\text{H}[\text{FeFe}]_{\text{H}}$, Figure 8c	−0.66	+0.72	−0.62	−0.64	0.04	
$\text{H}[\text{FeFe}]_{\text{H}}^{-1}$, Figure 8d	+0.43	+0.56	−0.65	−0.66	−0.01	
$\text{HH}[\text{FeFe}]_{\text{H}}$, Figure 8e	−0.44	+0.43	−0.55	−0.66	0.12	0.10

^a ΔN_{slab} ($\Delta N_{\text{cluster}}$) is the difference in electron number between adjacent configurations in the path, following the order of the table. The charges have been estimated by projection of the Kohn–Sham orbitals onto atomic wavefunctions.

Fe_d , and doubly hydrogenated Fe_d before desorption. The configuration at each of these stages is shown in Figure 7a–c, and values of the most relevant bond lengths are listed in Table 1. As electrons and protons are added during the course of the cycle, the electron numbers and the charge and spin distributions of course change. To quantify the changes, we projected the Kohn–Sham orbitals of the system onto appropriate atomic orbitals. The relevant atomic charges and electron number changes so obtained are listed in Table 2. Spin density contours are displayed in section S1 of the Supporting Information (SI) for the two odd-electron stages of the cycle.

The starting configuration is the neutral $\mu\text{-(CN)}_d\text{-H}$ with V-up described in the previous section and shown in Figures 6 and 7a. The HOMO of this configuration, Figure 8a.1, is formed by nonbonding t_{2g} -type d orbitals on the surface Fe atoms, the same as the HOMO of the clean surface.⁴³ On the other hand, the LUMO, d_{z^2} on each clean-surface Fe, is affected by the presence of the cluster. After functionalization, it is mostly localized on those surface Fe atoms, which are not linked to the cluster, cf. Figure 8a.2. The HOMO–LUMO gap is 0.16 eV. Fe_d and Fe_p have projected charges of $−0.56e$ and $−0.66e$, respectively, cf. Table 2. The total number of electrons is even, and there is no net spin.

We used the GGA+U method⁵³ to test the sensitivity of the results in Table 2 to the GGA functional we have used. We computed values of U for Fe in the pyrite slab and for Fe_d and Fe_p in the $[\text{FeFe}]_{\text{H}}$ cluster, both in vacuo, via the linear response method of Cococcioni and de Gironcoli,⁵⁴ finding 7.0 eV for the slab and 8.4 eV for both Fe_d and Fe_p . However, a value of 7.0 eV yields a poor value for the gap (much too large) and for the lattice constant of the clean

slab. A value of 3 eV instead yields an acceptable gap for the slab of 0.98 eV and does not affect the GGA lattice constant. We used this value of U for all Fe atoms in the functionalized slab. To obtain a value of U of 3.6 eV for both Fe_d and Fe_p in the supported cluster which would be consistent with that 3 eV value for the slab, we scaled up the latter by a factor of 1.2, the ratio of isolated cluster to

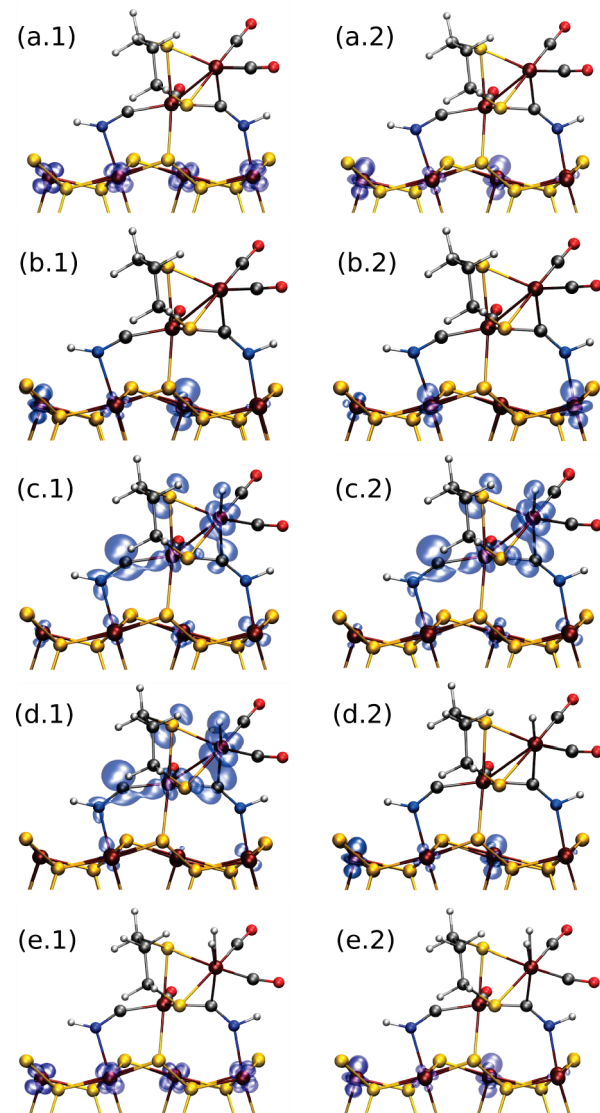


Figure 8. Optimized structures and HOMO (left panels, a–e.1) and LUMO (right panels, a–e.2) charge densities for the structures involved in the catalytic cycle of Table 2. (a) $[\text{FeFe}]_{\text{H}}$ neutral and (b) $[\text{FeFe}]_{\text{H}}^{-1}$ charged $−1$ isomers with a vacant coordination site on Fe_d . (c) $\text{H}[\text{FeFe}]_{\text{H}}$ neutral and (d) $\text{H}[\text{FeFe}]_{\text{H}}^{-1}$ charged $−1$ isomers with a H atom on Fe_d . (e) $\text{HH}[\text{FeFe}]_{\text{H}}$ neutral with Fe_d doubly hydrogenated. The contour value for plotting the electron density was 0.003. The color code is that of Figure 3.

clean slab values obtained by the linear response method.⁵⁴ Using these values of U , we recomputed the relevant atomic charges and electron-number changes entered in Table 2, which contains the GGA results from which we have inferred delocalization within the functionalized slab. The resulting charges and number changes are reported in Table S1 of the Supporting Information. They do not differ significantly (at most by 10%) from the entries in Table 2, demonstrating that the GGA is sufficiently accurate in this respect for our purposes.

Following the scheme of ref 29, we added one electron and one proton to the Fe_d of Figure 7a, resulting in the geometry of Figure 7b, H[FeFe]_H. From the computed energy difference between neutral systems [FeFe]_H and the resulting H[FeFe]_H, we obtained a hydrogen affinity for Fe_d of 15.41 eV. This addition is energetically less favorable than $\frac{1}{2}\text{H}_2$ by $\Delta E_1 = 0.44$ eV. Both the HOMO, which is singly occupied, and the spin-opposite LUMO are partially localized on the cluster, with 14% on Fe_d and 7% on Fe_p, cf. Figures 8c,1,2. With the HOMO density being roughly comparable on Fe_p and Fe_d, the Fe_p–Fe_d separation increases relatively little upon hydrogenation of Fe_d, from 2.52 to 2.57 Å. Before adding the proton to [FeFe]_H⁻¹, 74% of the added electron density resides on the slab and 19% on the cluster. [The shortfall of 7% is due to the shortcomings of the projection process.] Only 0.03 of an electron is added to Fe_d and none to Fe_p (Table 2). The remaining 16% is added primarily to the most electronegative ligands on Fe_d. The HOMO (LUMO) charge density is shown in Figure 8b.1 (Figure 8b.2). This delocalization of the electron distribution both within the complex formed by the Fe atoms and their ligands within the cluster and between the cluster and the slab mitigates against the use of the conventional notion of oxidation states and their changes for the iron atoms in this complex system. Upon adding the proton, only 2/3 of an electron is transferred from the slab to the cluster, while the proton picks up 0.96 of an electron, becoming a nearly neutral H atom, the remaining third coming largely from the electronegative ligands of Fe_d.

We next added a second proton and electron to the Fe_d–H of Figure 7b; the resulting optimized geometry is shown in Figure 7c. The hydrogen affinity is 15.99 eV, which means that this addition is energetically more favorable than $\frac{1}{2}\text{H}_2$ by $\Delta E_2 = -0.14$ eV. Upon addition of the second hydrogen to Fe_d, the Fe_p–Fe_d bond distance increases from 2.57 to 2.89 Å (cf. Table 1). Even though the individual Fe_d–H distances are 0.2 Å longer than that in the singly hydrogenated case, the η bond of the dihydrogen to Fe_d is strong and substantially breaks the Fe_p–Fe_d resonance, leading to this large additional opening of the Fe_p–Fe_d bond. The H–H distance of the two hydrogen atoms coordinated to Fe_d is 0.82 Å, which is only 0.07 Å larger than the computed distance of the isolated H₂ molecule. The HOMO and the LUMO are localized on the pyrite surface, essentially the same as for the configuration with a vacancy on Fe_d, cf. Figure 8e. Before adding the proton, cf. Figure 8d, 0.43 and 0.56 of the added electron goes to the slab and the cluster, respectively. Within the cluster, the added 0.56 is diffusely distributed over Fe_p, Fe_d, their electronegative ligands, and

the H atom. Upon adding the proton, only 0.44 of an electron transfers from the slab to the cluster, while nearly twice that much is transferred to the resulting second H atom. The balance is transferred from the first H on Fe_d (13%), Fe_d (10%), and its electronegative ligands. Both the H atoms on Fe_d are weakly positively charged. As above, within our computational framework, there is little evidence for the utility of the concept of classical oxidation states.

The last step of the cycle is H₂ desorption. We found that for this step no additional electron is needed: H₂ desorption from the neutral Fe_d–H₂ isomer of Figure 7c is an exothermic process with a $\Delta E = -(\Delta E_1 + \Delta E_2) = -0.30$ eV. Its activation energy barrier as computed with NEB³⁸ is only 0.07 eV, cf. Figure 7d. The barrier is low because of a near balance between the energy cost of breaking the η bond and the energy benefit from molecular bonding arising from decreasing the initially close approach of the H atoms. After desorption, the initial state with a vacancy on Fe_d is restored, Figure 7a, and a new cycle can start again.

4.2. H₂ Formation in Water. To investigate hydrogen production in water, we started by adding 37 H₂O molecules to the neutral isomer of Figure 7a. We then relaxed the system via damped dynamics, followed by an FPMD simulation at room temperature (RT) lasting 1.5 ps. We analyzed several configurations extracted from the simulation by computing the Kohn–Sham (KS) orbitals and by projecting them onto atomic wave functions. The HOMO–LUMO energy gaps in these configurations are in the range 0.34–0.49 eV, and both the HOMO and LUMO are almost entirely ($\sim 80\%$) localized on the Fe atoms of the pyrite surface. On the functionalized face of the slab, two of the eight surface Fe atoms within the unit cell are linked to the cluster; two under the cluster are inaccessible to the water, and water molecules are absorbed on the remaining four sites after the relaxation. They remain absorbed throughout the hydrogen production cycle described in the following.

First Protonation of Fe_d. After the equilibration described above, we added an electron to the electrode-cluster complex and a proton to a nearby water molecule close to the distal iron, forming a hydronium. The system remains globally neutral. Earlier,³⁰ we found that in dense water there is a competition between the diffusion of an H₃O⁺ toward Fe_d and the transfer of its proton away via the Grothuss-shuttle to the surrounding water molecules that solvate it. The diffusion toward Fe_d was energetically favorable, but proton exchange between water molecules was entropically favorable. The proton transfer away from the Fe_d was so rapid that we could not observe the less-frequent proton transfer to the site on the brief time scale of our simulations. This is the so-called “wandering proton” problem.⁵⁵ To simulate protonation of Fe_d, we biased the competition by constraining two of the three O–H bonds of the hydronium, leaving only one free to move, either to transfer away from or to protonate the Fe_d. Here, we constrained the hydronium in the same way. As the present focus is on learning how to modify the cluster for stable hydrogen production, we do not attempt here to determine the free energy barrier for protonation; we address that issue elsewhere.²⁷ During the 2.6 ps of an FPMD simulation at RT, the hydronium stayed close to

the distal iron, but the proton was not transferred to Fe_d . The distance between Fe_d and the unconstrained proton of the H_3O^+ fluctuated within 1.9–2.8 Å. This behavior suggests not only an entropic barrier but also the presence of an energy barrier that could not be overcome during our short simulation.

The HOMO is singly occupied and localized on the pyrite surface. However, the LUMO is partially localized on Fe_d . In a snapshot in which the distance between Fe_d and the closest H atom of the hydronium is 1.94 Å, 22% of the LUMO is on Fe_d . Accordingly, to enhance the rate of proton transfer to Fe_d , we added a second electron to a configuration taken from this FPMD simulation, changing the total charge to −1. We kept the constraints on two of the three O–H bonds of the hydronium and observed proton transfer to Fe_d after 1.5 ps of an FPMD simulation at RT lasting 3.6 ps. After protonation, the system was stable; the proton remained on Fe_d . We found that the presence of the hydronium close to the cluster stabilized an increased negative charge of Fe_d before the protonation. From an analysis of five configurations extracted from this simulation with distances of the nearest H of the hydronium to Fe_d in the range range 2.36–2.68 Å, we found that about 25% of the HOMO was on Fe_d . The HOMO (doubly occupied) is in the gap, about 0.2 eV above the next valence state and 0.1 eV below the pyrite conduction bands. We also analyzed several configurations extracted from an FPMD simulation at RT lasting 2.2 ps with the supported catalyst charged −2 and immersed in *neutral* water. Without the hydronium ion, the extra charge was delocalized on the Fe atoms of the surface. From all of the above evidence, we conclude that the hydrogenation of Fe_d occurs via coordinated electron and proton transfers to Fe_d .

We repeated the simulation starting from a slightly different initial configuration with charge −1 and observed the protonation of Fe_d after 0.6 ps of a simulation lasting 1.1 ps. However, without constraining the bond lengths of the H_3O^+ ion, the proton was instead transferred to a nearby water molecule and solvated. The hydronium stayed 4–5 Å away from Fe_d for the duration of the simulation, 3.1 ps. At this larger distance, the hydronium did not stabilize the charge on Fe_d . Occasionally, depending on the configuration, a small contribution of Fe_p and Fe_d (less than 5% each) to the HOMO was observed. In contrast, when the hydronium is close to Fe_d , the HOMO amplitude on the Fe_d is significant. This observation suggests that the catalytic reaction will be constrained by proton diffusion and that the diffusion rate will be significantly affected by the potential energy surface experienced by the proton near the surface of the functionalized electrode.

To investigate further the effects produced by the presence of the hydronium on the charge distribution in the cluster, we removed the hydronium from a configuration selected before the proton transfer to Fe_d and computed the KS orbitals of the resulting system (which has a charge of −2). The HOMO was partially located on Fe_d (13%), with its remainder mostly on the surface. We equilibrated the system starting from this configuration and observed a rapid decrease of the contribution of Fe_d to the HOMO. In less than 0.6 ps,

the HOMO was localized entirely on the pyrite surface. This suggests that the presence of a H_3O^+ close to Fe_d induces, in addition to its attractive electrostatic potential, a structural modification of the supported cluster which contributes to stabilization of the charge on Fe_d . After the removal of the hydronium, time is required for the system to relax and for the charge to transfer back to the slab. We found the same effect in vacuo by removing the water molecules as well as the hydronium ion from the snapshot discussed above. In summary, we found that *two* additional electrons are required to lower the energy barrier involved in the proton transfer, and that the presence of the hydronium is required to stabilize the charge on the distal iron.

Second Protonation of Fe_d and H_2 Production. After protonation of Fe_d , we equilibrated the system for 2.1 ps at RT and then introduced a second proton into the water, neutralizing the system. In the starting configuration, the distance between the O atom of the H_3O^+ and Fe_d was 4.4 Å. The proton diffused very rapidly toward the $\text{Fe}_d\text{--H}$. Transfer of the H^+ to the $\text{Fe}_d\text{--H}$ was followed by H_2 desorption, the supported catalyst remaining neutral. When Fe_d is singly protonated and the system is in the neutral $\text{H}[\text{FeFe}]_{\text{H}}$ configuration, the H atom on Fe_d is essentially neutral, cf. Table 2 for the vacuum case. When a single electron is added prior to the addition of a second proton to the water, creating the $\text{H}[\text{FeFe}]_{\text{H}}^{-1}$ configuration, that H atom remains essentially neutral (compare Table 2). Nevertheless, in the presence of a chain of water molecules which connects the solvated hydronium to the $\text{Fe}_d\text{--H}$ (with the final molecule of the chain having one of its H atoms close to and spontaneously coordinated with the protruding H atom), the protonation occurs via the fast Grotthuss-like diffusion of H^+ directly toward Fe_d driven by a transfer of an electron which is coordinated with the motion of the proton. The transfer comes in part from the electrode and in part from the electronegative ligands bonded to Fe_d . The resulting H_2 molecule is η -coordinated with Fe_d in the $\text{HH}[\text{FeFe}]_{\text{H}}$ configuration and is weakly positively charged (compare Table 2). The total charge on Fe_d and Fe_p remains unchanged, the electron deficiency on the $\eta\text{-H}_2$ arising from charge flowing from it to the electronegative ligands of Fe_d . Conversely, the bare Fe_d , either in the neutral $[\text{FeFe}]_{\text{H}}$ configuration or in the negatively charged $[\text{FeFe}]_{\text{H}}^{-1}$ configuration, does not coordinate with an H_2O molecule because of (i) Coulomb repulsion between the lone pair of the O atom and the negative charge on Fe_d in both configurations (cf Table 2), (ii) the Pauli repulsion associated with formation and occupation of an antibonding σ orbital between the d_z^2 orbital of the vacant coordination site and the overlapping sp^3 -like lone pair orbitals of the oxygen, and (iii) the cost of modifying the H-bond network of the water. This reduces the rate of the first protonation of Fe_d , which, as pointed out in ref 30, is the bottleneck of the cycle because it occurs only after the diffusion of a partially unsolvated H_3O^+ toward Fe_d to a distance short enough for a proton transfer (<2 Å). Once the $\text{Fe}_d\text{--H}$ bond is formed in $\text{H}[\text{FeFe}]_{\text{H}}$, however, effect ii is no longer in play, and the lowering in energy arising from sharing the electron of that H with an H atom of a water molecule together with that from the transfer of

the additional electron is strong enough to overcome effect iii, as we have observed in the 2.1 ps simulation referred to above.

We repeated the simulation of the second protonation of Fe_d by changing the initial position of the additional proton introduced in water. Here, the initial distance between the O atom of the H_3O^+ and Fe_d was 5.6 Å. From this configuration, the proton diffused away from Fe_d . After about 0.7 ps, the hydronium was within 4 Å of the S_{chel} exposed to the water. The proton remained in the water as H_3O^+ at distances shorter than 4 Å from this sulfur for the remaining 2.3 ps of an FPMD at RT lasting 3.0 ps. From these results, we can draw two conclusions. First, there is only a small subset of reaction pathways along which barrier-free adsorption of a second proton and subsequent hydrogen production can occur. Second, there are local configurations in which the second proton can be at least temporarily trapped, e.g., near S_{chel} in the second simulation, reducing the overall catalytic efficiency, as is the case also for the first protonation. This apparent attraction of S_{chel} for the proton turns out to have serious consequences, as discussed below.

5. An Instability of the Supported $[\text{FeFe}]_H$ Cluster: $[\text{FeFe}]_P$ as a Remedy

Thus far, we have focused on hydrogen production at a vacant coordination site on Fe_d . However, the S atom of PDT further from the surface, S_{chel} , turns out to be readily protonated. We explore in subsection 5.1 the negative consequences of that protonation for the stability of the cluster both *in vacuo* and in water and consequently for hydrogen production. In subsection 5.2, we describe a further modification of the cluster which eliminates that difficulty.

5.1. Protonation of S_{chel} Opens the PDT Bridge. Calculations *in vacuo* show that protonation of the S atom of PDT furthest from the surface (S_{chel}) breaks the $\text{Fe}_p-\text{S}_{\text{chel}}$ bond, opening the bridge and exposing a bridging site between the two Fe's of the cluster. The resulting configuration, Figure 9a, is lower in energy than that of Fe_d-H by 0.07 eV when the system is neutral. Transfer of the H atom from S_{chel} to the vacant site on Fe_d would restore the catalytic cycle discussed in the previous section, but the corresponding energy barrier computed in *vacuo* via NEB is quite high, 0.68 eV. Starting from this configuration with S_{chel} protonated, we added one electron and one proton to Fe_d , producing the configuration in Figure 9b. This configuration is less stable than that with both protons on Fe_d by 0.26 eV. However, the energy barrier to transferring a H atom from S_{chel} to Fe_d when a proton is already present on Fe_d is 0.61 eV. Such a high barrier would make H_2 production very inefficient.

We also added an electron and a proton to Fe_p in the open configuration of Figure 9a. The optimized geometry, Figure 9c, is similar to the $\mu\text{-H}$ configuration explored previously.^{29,30} A H atom bridges Fe_p and Fe_d . The energy is lower than for two H atoms on Fe_d by 0.52 eV, Figure 7c. The presence of $\mu\text{-H}$ would make H_2 production after adding another H to Fe_p very inefficient because of a large H_2 desorption barrier arising from strong dihydrogen bonding (see below), as found earlier.^{29,30}

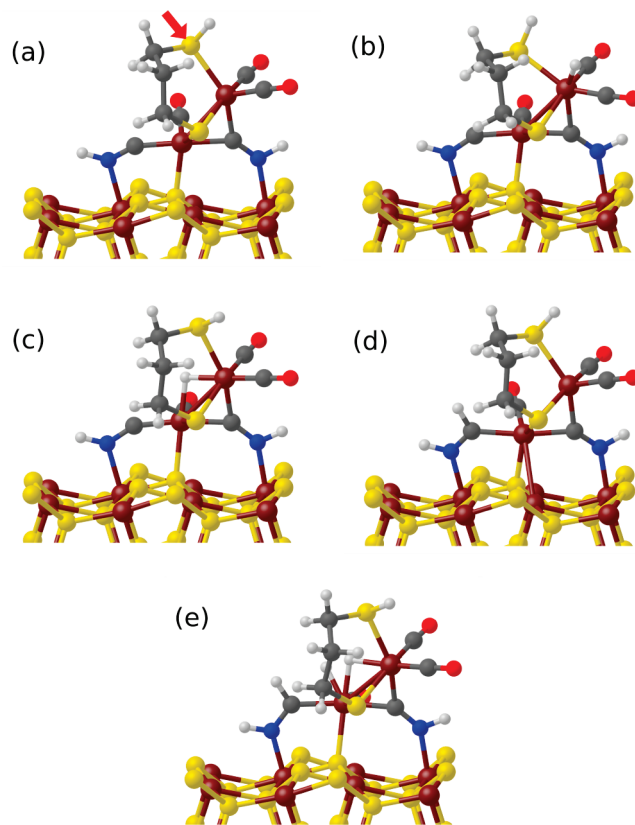


Figure 9. Configurations corresponding to alternative pathways involving the protonation of the S_{chel} atom of the PDT. These neutral isomers were optimized in *vacuo*. (a) Geometry of the supported catalyst with a hydrogen atom connected to the S_{chel} , indicated by the red arrow. The protonation breaks the $\text{Fe}_p-\text{S}_{\text{chel}}$ bond. The resulting configuration is lower in energy than that of the Fe_d-H of Figure 7b by 0.07 eV. (b) Geometry with S_{chel} and Fe_d hydrogenated. (c) Geometry with an H atom bridging Fe_p and Fe_d ($\mu\text{-H}$), and S_{chel} hydrogenated. (d) Geometry with the C atom of the $(\text{CN})_p-\text{H}$ group protonated. (e) Geometry with one H atom bridging Fe_p and Fe_d ($\mu\text{-H}$), a second H atom on Fe_p , and as in d the C atom of the $(\text{CN})_p-\text{H}$ group protonated. The color code is that of Figure 3.

In water, protonation of S_{chel} was observed for a configuration where the supported catalyst was charged -2 and had a vacancy on Fe_d . The O atom of the hydronium ion was located at 4.85 Å and 3.93 Å from Fe_d and S_{chel} , respectively. We constrained all three O–H bond lengths of the H_3O^+ to prevent proton diffusion and observed displacement of S_{chel} toward the hydronium driven by electrostatic interaction. After removal of one of the three constraints in the H_3O^+ , displacement of S_{chel} breaks the $\text{Fe}_p-\text{S}_{\text{chel}}$ bond, whose length increases up to about 4 Å. Simultaneously, the proton approaches S_{chel} along the line linking it with Fe_p . The main bond lengths involved in the reaction are plotted as function of time in Figure 10. S_{chel} becomes 2-fold coordinated and accepts a proton from the hydronium. The outcome of this reaction is an opened structure with the chelating group displaced toward Fe_d , resulting in reduction of the empty space associated with the vacant site. The corresponding structure optimized in *vacuo* (cf. Figure 9a) has a lower energy than that with a

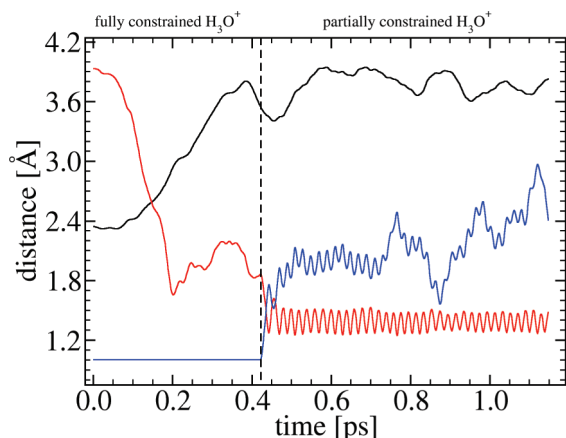


Figure 10. Plot of the $\text{Fe}_p\text{--S}_{\text{chel}}$ (black line), $\text{S}_{\text{chel}}\text{--H}$ (red line), O–H (blue line) bond length [\AA] as a function of time [ps]. The FPMD simulation at RT was divided into two parts separated by the vertical dotted line at about 0.4 ps. In the first part, lasting about 0.4 ps, all three O–H bond lengths of the hydronium were constrained (fully constrained H_3O^+). The $\text{Fe}_p\text{--S}_{\text{chel}}$ bond broke (black line), and the hydronium moved toward S_{chel} (red line). When the constraint on the closest H atom of the hydronium to S_{chel} was removed (partially constrained H_3O^+), the proton transferred to S_{chel} .

proton on Fe_d (cf. Figure 7b and section 4) by 0.67 eV (neutral) and 0.21 eV (charged –1).

The protonation of S_{chel} strongly affects the structure of the catalyst. It opens the structure and creates an undercoordinated Fe_p that could be protonated. It also reduces the empty space available to the vacancy on Fe_d , making its protonation more difficult. To examine the consequences of these potentially unfavorable changes, we explored the reactivity of the cluster with S_{chel} protonated in acidified water. We performed two FPMD simulations at RT in water containing one hydronium ion differing in its initial position. In one case, the H_3O^+ was close to Fe_p , and in the other, it was close to Fe_d . In neither case did a proton transfer to the Fe atom when the charge was –1 or –2. For Fe_p , the C atom of the $(\text{CN})_p\text{--H}$ was protonated instead, producing the isomer in Figure 9d. Nevertheless, we optimized the geometry for a dihydrogen at Fe_p in vacuo, Figure 9e, resulting in one H in the μ -bridging position and one H on Fe_p . The resulting energy is lower by 0.31 eV than that after desorption, suggesting that this channel for H_2 production would be inefficient in water. Adding an additional electron makes desorption of H_2 an exothermic process by 0.20 eV, but the activation energy barrier of 0.47 eV is too large for an efficient turnover. For Fe_d , we attribute the reduction of the reactivity of its vacant site to the compression of the space around it and the consequent decrease in electron density.

In summary, S_{chel} can be protonated along very specific pathways in vacuo, pathways consistent with elementary ligand-field theory. In water, the $\text{Fe}_p\text{--S}_{\text{chel}}$ bond opens in the process of the protonation of S_{chel} along similar pathways. With S_{chel} protonated, all H_2 production pathways either are very inefficient in themselves and would reduce the overall efficiency of the catalyst due to large barriers or would lead to destruction of the catalyst. As we demonstrated in section

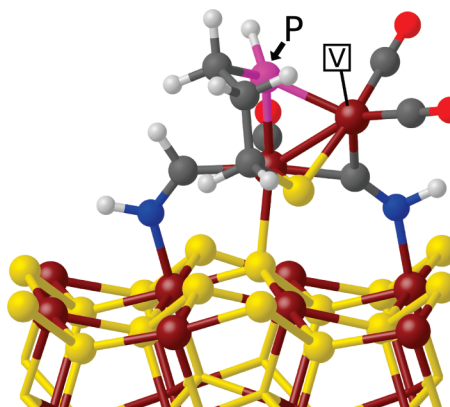


Figure 11. Side view of the $[\text{FeFe}]_p$ cluster linked to the FeS_2 (100) surface in the same way as the $[\text{FeFe}]_H$ cluster in Figure 5. The S_{chel} of $[\text{FeFe}]_H$ is replaced by a PH group. The distal iron has a vacant site, indicated by V. The color code is that of Figure 3.

4.2 that the supported catalyst produces hydrogen efficiently when its chelating bridge is intact, the next task is to find a modification of the cluster which stabilizes its chelating bridge.

5.2. Introducing $[\text{FeFe}]_p$. Opening of the chelating bridge must be avoided. The opening is a consequence of the inability of the sulfur atom S_{chel} to maintain four strong covalent bonds after the protonation that will inevitably occur upon exposure to acidified water. The weakest of the four, its bond to Fe_p , breaks and opens the bridge. The $\text{S}_{\text{chel}}\text{--Fe}_p$ bond is weak because it lies opposite of the strong $\text{Fe}_p\text{--S}_{\text{surf}}$ bond along one of the quasi-octohedral coordination axes of Fe_p , which withdraws electron density from it. The $\text{Fe}_p\text{--S}_{\text{surf}}$ bond is strong because it restores the bulk 4-fold coordination of S_{surf} . Clearly, one needs to replace S_{chel} by a group stereochemically similar to a sulfur to minimize structural distortion of the cluster and distortion of its electron density, yet capable of sustaining or being protected from protonation as well as forming the three strong bonds required for anchoring the bridge to the di-iron. The group P–H can be regarded as an approximation to sulfur and could satisfy the minimum distortion requirement. Its phosphorus atom is also capable of forming the three strong bonds needed to anchor the PDT bridge to the di-irons. Substitution of P–H for S_{chel} yields the $[\text{FeFe}]_p$ cluster shown in Figure 11 stably attached to the pyrite surface. We have carried out computations on hydrogen production in vacuo and in water by $[\text{FeFe}]_p$. We find that it remains stably attached to the electrode and intact throughout a successful hydrogen production cycle, as reported in detail elsewhere.²⁷

6. Discussion and Conclusions

Our goal in this work was to find a conformation of the $[\text{FeFe}]_H$ cluster which would (1) link stably to the (100) surface of pyrite while (2) retaining a vacant coordination site on Fe_d at which H_2 could be produced readily in acidified H_2O . We started by mimicking the sulfur link between Fe_p and an Fe of the Fe_4S_4 cubane in the enzyme by inserting a sulfur between the Fe_p of the naked cluster and a surface Fe. However, the $\text{Fe}_p\text{--S}$ link broke in water upon proton-

ation, just as the methylthiol–Fe_p link did in water in the absence of the surface.³⁰ Next, we linked Fe_p directly to a surface S atom, eliminating the S intermediary but still mimicking the linkage in the enzyme. The resulting complex was stable only in the CO_T configuration, which could not produce hydrogen efficiently. We inferred that the difference between the enzyme environment and that of a pyrite surface exposed to water was too great for the twin requirements 1 and 2 to continue to be met by a linking sulfur, and we abandoned the notion of that biomimetic linkage.

One possible solution would be to use for coupling to the surface a ligand of the di-irons already in the μ -bridging position. The μ -CO of the native configuration could not serve as that ligand, but we had observed an unusual novel structure with the protonated (CN)_d moved into the bridging position during an FPMD simulation at $T = 300\text{--}350\text{ K}$ in water,³⁰ Figure 5 (inset). To allow the N of that μ -(CN)_d–H to come close enough to the surface to form a dative bond with a surface Fe atom, we shifted the (CN)_p–H into the coordination site formerly occupied by the methylthiol in the cluster of refs 29 and 30, freeing Fe_p to bond to a surface S atom at the vacated coordination site. The N of the (CN)_p–H forms a dative bond with another surface Fe atom, creating a strong, stable tridentate support on the surface, Figure 5, with the vacant coordination site preserved at Fe_d, meeting requirement 1 and opening the possibility that requirement 2 could be met. The DTMA bridge used in refs 29 and 30 was replaced by a PDT bridge, with a further increase in stability.

In our first study of hydrogen production in *vacuo*,²⁹ we simply added both electrons and protons to the cluster by fiat. In our second study,³⁰ protons were introduced more realistically, migrating through the water via the Grotthuss-shuttle mechanism,⁵² while electrons were still simply added by fiat. In the present work, the electrons were added to the entire surface/ μ -(CN)_d–H cluster complex. The relevant LUMO before addition and HOMO after addition of an electron at the various stages of the hydrogen producing cycle were localized primarily on the pyrite surface before the approach of a proton to Fe_d. As the proton–Fe_d distance shrank, the HOMO shifted primarily to Fe_d. After protonation, the first hydrogen projected outward into the water and coordinated with the H of the closest water molecule, providing a channel along which the second proton could approach by the Grotthuss mechanism to form the second hydrogen. This demonstrates that both electron transfer from the FeS₂ slab to the μ -(CN)_d–H cluster and proton transfer from the water can take place, the essential steps in modeling hydrogen production.

As found in our previous study,³⁰ transfer of the first proton from the water to Fe_d is the bottleneck in the H₂-production cycle because of its competition with rapid proton diffusion away via the Grotthuss-shuttle. To observe that proton transfer within the picosecond time scale of our simulations, we constrained two of the OH bonds of the neighboring hydronium. No constraint was needed for the second because the projecting H of the first Fe_d–H complex coordinated with the H of a neighboring water molecule, providing a path for transfer of the second proton to Fe_d via

the Grotthuss mechanism. Desorption of the resulting H₂ was then observed during our picosecond-scale simulations, demonstrating H₂ production by the supported cluster, meeting requirements 1 and 2.

That did not complete the story, however. We observed very specific configurations of a hydronium ion neighboring S_{chel} which both weaken the Fe_p–S_{chel} bond, breaking it and allowing spontaneous proton transfer to S_{chel}. When that H of the hydronium which is closest to S_{chel} approaches it along or near the direction of the bond joining it to Fe_p, the Fe_p–S_{chel} bond lengthens and then opens as the bond switches from Fe_p to H, forming a thiol. These pathways are consistent with expectations from elementary valence-bond theory. The PDT chelating bridge decouples from Fe_p, opening a channel of proton access to the di-iron from the water and allowing for the possibility of the binding of two hydrogen atoms in a bridging configuration there, in agreement with calculations by Felton et al.^{23,24} on an analogous open-bridged cluster in a vacuum. These authors also observed hydrogen production experimentally with that cluster as a catalyst and, on the basis of their computations, attributed it to hydrogen formation at and desorption from the di-iron bridging site. They did not determine the barrier to desorption, however. We have found the barrier to desorption of H₂ in *vacuo* from the di-iron bridging site of a CO_T configuration to be 0.47 eV–0.54 eV depending on the cluster configuration. This should be a reasonable estimate for the barrier to desorption of a di-iron bridging, H-atom pair within our μ -(CN)_d–H cluster when its chelating PDT bridge is opened by protonation of S_{chel}. Moreover, we have found the desorption of H₂ from the open configuration when a dihydrogen is at Fe_p to be inhibited by an activation energy barrier of 0.47 eV. Should the cluster remain in the open configuration for a significant fraction of the time, its performance as a catalyst would be degraded or the catalyst would even be destroyed.

This opening of the chelating bridge must be avoided. The opening is a consequence of the inability of the sulfur atom S_{chel} to maintain four strong covalent bonds after the protonation that will inevitably occur upon exposure to acidified water. The weakest of the four, its bond to Fe_p, breaks and opens the bridge. As discussed briefly in section 5.2, substituting a P–H group for S_{chel} solves that problem, creating the [FeFe]_P cluster as a viable model catalyst for the electrocatalytic production of hydrogen. We report elsewhere a detailed analysis of hydrogen production by [FeFe]_P.²⁷ Moreover, substitution of other moieties for the H of the P–H allows for fine-tuning of the catalytic activity. In particular, it opens the possibility of reduction of the free-energy barrier to first protonation, the bottleneck in the production cycle.

In conclusion, we have presented extensive FPMD simulations of hydrogen production by a coupled catalyst–electrode system consisting of a modified [FeFe]_H cluster supported on a FeS₂(100) surface in acidified water, a system far more complex than those typically treated by first principles methods. The principal findings of the present study are as follows: (i) A stable thiol link analogous to that in the enzyme cannot be made between the unmodified [FeFe]_H cluster and the pyrite surface. (ii) A modified μ -(CN)_d–H isomer of the

$[\text{FeFe}]_{\text{H}}$ cluster forms a stable, tridentate link to the surface. (iii) There is a low-activation-energy pathway for hydrogen production from acidified water by the functionalized pyrite surface. (iv) The electrons in the electrode and the protons in the water attract each other to the catalyst in the first hydrogenation of Fe_d . (v) That di-iron bridging sulfur which is exposed to the water develops a weak link to Fe_p upon its protonation, but replacing it with a P–H group eliminates this instability²⁷ (vi) Facile electrocatalytic hydrogen production is feasible by this modified-cluster/pyrite system. To achieve these results, we have employed the first principles molecular dynamics method at an advanced level of system complexity and have illustrated thereby the utility and power of FPMD for molecular design.

Acknowledgment. This work was supported by the Department of Energy, Office of Basic Energy Sciences, Division of Materials Sciences and Engineering under Award DE-FG02-06ER-46344. This research used resources of the National Energy Research Scientific Computing Center, which is supported by the Office of Science of the U.S. Department of Energy under Contract No. DE-AC02-05CH11231. The simulations presented in this article were in part performed on computational resources supported by the PICSciE-OIT High Performance Computing Center and Visualization Laboratory. We thank Patrick Sit for discussion of the GGA+U method.

Supporting Information Available: Figures S1 and S2 display the electron-spin density contours in the two odd-electron configurations of the cycle, $[\text{FeFe}]_{\text{H}}^{-1}$ and $\text{H}[\text{FeFe}]_{\text{H}}$, respectively. Table S1 contains the relevant charges and electron number changes in the intermediates of the H_2 production cycle in vacuo obtained via GGA+U for comparison with the corresponding GGA results in Table 2. This material is available free of charges via the Internet at <http://pubs.acs.org/>.

References

- Vignais, P. M.; Billoud, B.; Meyer, J. *FEMS Microbiol. Rev.* **2001**, *25*, 455.
- Fontecilla-Camps, J. C.; Volbeda, A.; Cavazza, C.; Nicolet, Y. *Chem. Rev.* **2007**, *107*, 4273.
- Bruschi, M.; Greco, C.; Kaukonen, M.; Fantucci, P.; Ryde, U.; De Gioia, L. *Angew. Chem., Int. Ed.* **2009**, *48*, 3503.
- Cao, Z. X.; Hall, M. B. *J. Am. Chem. Soc.* **2001**, *123*, 3734.
- Liu, Z. P.; Hu, P. *J. Am. Chem. Soc.* **2002**, *124*, 5175.
- Bruschi, M.; Fantucci, P.; De Gioia, L. *Inorg. Chem.* **2002**, *41*, 1421.
- Greco, C.; Bruschi, M.; De Gioia, L.; Ryde, U. *Inorg. Chem.* **2007**, *46*, 5911.
- Fiedler, A. T.; Brunold, T. C. *Inorg. Chem.* **2005**, *44*, 9322.
- Zilberman, S.; Stiefel, E. I.; Cohen, M. H.; Car, R. *J. Phys. Chem. B* **2006**, *110*, 7049.
- Szilagyi, R. K.; Winslow, M. A. *J. Comput. Chem.* **2006**, *27*, 1385.
- Liu, T. B.; Li, B.; Singleton, M. L.; Hall, M. B.; Daresbourg, M. Y. *J. Am. Chem. Soc.* **2009**, *131*, 8296.
- Siegbahn, P. E. M.; Tye, J. W.; Hall, M. B. *Chem. Rev.* **2007**, *107*, 4414.
- Fan, H. J.; Hall, M. B. *J. Am. Chem. Soc.* **2001**, *123*, 3828.
- Cracknell, J. A.; Vincent, K. A.; Armstrong, F. A. *Chem. Rev.* **2008**, *108*, 2439.
- Tye, J. W.; Hall, M. B.; Daresbourg, M. Y. *Proc. Natl. Acad. Sci. U.S.A.* **2005**, *102*, 16911.
- Tard, C.; Liu, X. M.; Ibrahim, S. K.; Bruschi, M.; De Gioia, L.; Davies, S. C.; Yang, X.; Wang, L. S.; Sawers, G.; Pickett, C. J. *Nature* **2005**, *433*, 610.
- Peters, J. W.; Lanzilotta, W. N.; Lemon, B. J.; Seefeldt, L. C. *Science* **1998**, *282*, 1853.
- Nicolet, Y.; de Lacey, A. L.; Vernede, X.; Fernandez, V. M.; Hatchikian, E. C.; Fontecilla-Camps, J. C. *J. Am. Chem. Soc.* **2001**, *123*, 1596.
- Vincent, K. A.; Cracknell, J. A.; Lenz, O.; Zebger, I.; Friedrich, B.; Armstrong, F. A. *Proc. Natl. Acad. Sci. U.S.A.* **2005**, *102*, 16951.
- Nicolet, Y.; Piras, C.; Legrand, P.; Hatchikian, C. E.; Fontecilla-Camps, J. C. *Struct. Fold. Des.* **1999**, *7*, 13.
- Lubitz, W.; Reijerse, E.; van Gastel, M. *Chem. Rev.* **2007**, *107*, 4331.
- Reisner, E.; Fontecilla-Camps, J. C.; Armstrong, F. A. *Chem. Commun.* **2009**, 550.
- Felton, G. A. N.; Vannucci, A. K.; Chen, J. Z.; Lockett, L. T.; Okumura, N.; Petro, B. J.; Zakai, U. I.; Evans, D. H.; Glass, R. S.; Lichtenberger, D. L. *J. Am. Chem. Soc.* **2007**, *129*, 12521.
- Felton, G. A. N.; Vannucci, A. K.; Okumura, N.; Lockett, L. T.; Evans, D. H.; Glass, R. S.; Lichtenberger, D. L. *Organometallics* **2008**, *27*, 4671.
- Hamberger, M.; Gervaldo, M.; Svedruzic, D.; King, P. W.; Gust, D.; Ghirardi, M.; Moore, A. L.; Moore, T. A. *J. Am. Chem. Soc.* **2008**, *130*, 2015.
- Car, R.; Parrinello, M. *Phys. Rev. Lett.* **1985**, *55*, 2471.
- Zipoli, F.; Car, R.; Cohen, M. H.; Selloni, A. *J. Am. Chem. Soc.* **2010**, *132*, 8593.
- Liu, Z. P.; Hu, P. *J. Am. Chem. Soc.* **2002**, *124*, 11568.
- Sbraccia, C.; Zipoli, F.; Car, R.; Cohen, M. H.; Dismukes, G. C.; Selloni, A. *J. Phys. Chem. B* **2008**, *112*, 13381.
- Zipoli, F.; Car, R.; Cohen, M. H.; Selloni, A. *J. Phys. Chem. B* **2009**, *113*, 13096.
- Perdew, J. P.; Burke, K.; Ernzerhof, M. *Phys. Rev. Lett.* **1997**, *78*, 1396.
- Giannozzi, P.; Baroni, S.; Bonini, N.; Calandra, M.; Car, R.; Cavazzoni, C.; Ceresoli, D.; Chiarotti, G. L.; Cococcioni, M.; Dabo, I.; Dal Corso, A.; de Gironcoli, S.; Fabris, S.; Fratesi, G.; Gebauer, R.; Gerstmann, U.; Gougoissis, C.; Kokalj, A.; Lazzeri, M.; Martin-Samos, L.; Marzari, N.; Mauri, F.; Mazzarello, R.; Paolini, S.; Pasquarello, A.; Paulatto, L.; Sbraccia, C.; Scandolo, S.; Sclauzero, G.; Seitsonen, A. P.; Smogunov, A.; Umari, P.; Wentzcovitch, R. M. *J. Phys.: Condens. Matter* **2009**, *21*, 395502.
- Vanderbilt, D. *Phys. Rev. B* **1990**, *41*, 7892.
- Laasonen, K.; Pasquarello, A.; Car, R.; Lee, C.; Vanderbilt, D. *Phys. Rev. B* **1993**, *47*, 10142.
- Finklea, S. L.; Cathey, L.; Amma, E. L. *Acta Crystallogr., Sect. A* **1976**, *32*, 529.

- (36) Nosé, S. *J. Chem. Phys.* **1984**, *81*, 511.
- (37) Blöchl, P. E.; Parrinello, M. *Phys. Rev. B* **1992**, *45*, 9413.
- (38) Henkelman, G.; Uberuaga, B. P.; Jónsson, H. *J. Chem. Phys.* **2000**, *113*, 9901.
- (39) E, W. N.; Ren, W. Q.; Vanden-Eijnden, E. *Phys. Rev. B* **2002**, *66*, 052301.
- (40) Nair, N. N.; Schreiner, E.; Marx, D. *J. Am. Chem. Soc.* **2006**, *128*, 13815.
- (41) Stirling, A.; Bernasconi, M.; Parrinello, M. *Phys. Rev. B* **2007**, *75*, 165406.
- (42) Stirling, A.; Bernasconi, M.; Parrinello, M. *J. Chem. Phys.* **2003**, *119*, 4934.
- (43) Stirling, A.; Bernasconi, M.; Parrinello, M. *J. Chem. Phys.* **2003**, *118*, 8917.
- (44) Ferrer, I. J.; Nevskaia, D. M.; Delasheras, C.; Sánchez, C. *Solid State Commun.* **1990**, *74*, 913.
- (45) Schreiner, E.; Nair, N. N.; Marx, D. *J. Am. Chem. Soc.* **2008**, *130*, 2768.
- (46) Boehme, C.; Marx, D. *J. Am. Chem. Soc.* **2003**, *125*, 13362.
- (47) Rodriguez, J. A.; Abreu, I. A. *J. Phys. Chem. B* **2005**, *109*, 2754.
- (48) Kendelewicz, T.; Doyle, C. S.; Bostick, B. C.; Brown, G. E. *Surf. Sci.* **2004**, *558*, 80.
- (49) Rosso, K. M.; Becker, U.; Hochella, M. F. *Am. Mineral.* **1999**, *84*, 1549.
- (50) Rickard, D.; Luther, G. W. *Chem. Rev.* **2007**, *107*, 514.
- (51) Murphy, R.; Strongin, D. R. *Surf. Sci. Rep.* **2009**, *64*, 1.
- (52) Marx, D.; Tuckerman, M. E.; Hutter, J.; Parrinello, M. *Nature* **1999**, *397*, 601.
- (53) Anisimov, V. I.; Zaanen, J.; Andersen, O. K. *Phys. Rev. B* **1991**, *44*, 943.
- (54) Cococcioni, M.; de Gironcoli, S. *Phys. Rev. B* **2005**, *71*, 35105.
- (55) Leung, K.; Nielsen, I. M. B.; Criscenti, L. J. *J. Am. Chem. Soc.* **2009**, *131*, 18358.

CT100319B